ACS Photonics
Article
pubs.acs.org/journal/apchd5

Spanning Strong to Weak Normal Mode Coupling between Vibrational and Fabry–Pérot Cavity Modes through Tuning of Vibrational Absorption Strength

B. S. Simpkins,*[†] Kenan P. Fears,[†] Walter J. Dressick,[‡] Bryan T. Spann,[†,§] Adam D. Dunkelberger,[†,§] and Jeffrey C. Owrutsky[†]

[†]Chemistry Division and [‡]Center for Bio/Molecular Science and Engineering, Naval Research Laboratory, 4555 Overlook Avenue SW, Washington, D.C. 20375, United States

Ⓢ *Supporting Information*

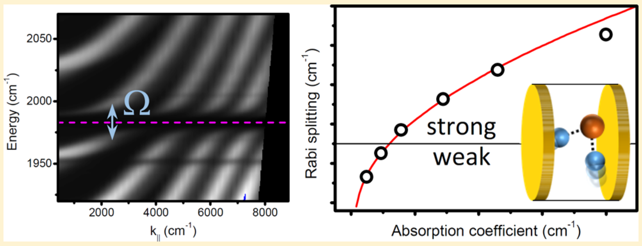

ABSTRACT: Designing coupled vibrational-cavity polariton systems to modify chemical reaction rates and paths requires an understanding of how this coupling depends on system parameters (i.e., absorber strength, modal distribution, and vibrational absorber and cavity line widths). Here, we evaluate the impact of absorption coefficient and cavity design on normal mode coupling between a Fabry–Pérot cavity and a molecular vibration. For a vibrational band of urethane in a polymer matrix, the coupling strength increases with its concentration so that the system spans the weak and strong coupling regimes. The experimentally determined Rabi splitting values are in excellent agreement with an analytical expression derived for classical coupled oscillators that includes no fitting parameters. Also, the cavity mode profile is altered through choice of mirror type, with metal mirrors resulting in stronger confinement and thus coupling, while dielectric stack mirrors provide higher transmission for a given cavity quality factor and decreased coupling due to greater mode penetration into the dielectric mirror. In addition to polymers, the cavities can couple to molecular vibrational bands of dissolved species in solution, which greatly expands the range of systems that can be explored. Finally, longer path length cavities are used to demonstrate the path length independence of the coupling strength. The ability to adjust the cavity line width, through the use of higher order modes, represents a route to match the cavity dephasing time to that of the molecular vibration and may be applied to a range of molecular systems. Understanding the roles of cavity design and validating empirical and analytical descriptions of absorber properties on coupling strength will facilitate application of these strong coupling effects to enable currently unreachable chemistries.

KEYWORDS: *quantum optical chemistry, vacuum Rabi splitting, strong coupling, infrared spectroscopy, optical cavity, vibrational coupling*

Coupling between an optically driven material excitation (e.g., a semiconductor quantum dot excitonic absorption) and a confined optical mode (e.g., an optical microcavity) can drastically alter the behavior of both modes. Strong coupling, which occurs when the two modes are in resonance and the interaction between the two exceeds the damping rate, produces two hybridized states whose fundamental character is a quantum-mechanical superposition of the two original modes. Each of these mixed-character eigenstates is shifted from the original resonant frequency by half the Rabi splitting, Ω.[1] Such coupled systems are variously referred to as cavity polaritons,[2] coupled normal modes,[1] plexcitons,[3] or simply coupled modes. If the system consists of a single quantum oscillator (two-level atom, single quantum dot, etc.) interacting with a single cavity photon, nonlinear effects such as photon blocking and climbing of the Jaynes–Cummings ladder may occur. The splitting in such a system is referred to as *vacuum* Rabi splitting[1,4,5] as opposed to simply Rabi or polariton splitting associated with ensembles of individual oscillators, as described herein. Relaxation lifetimes,[6,7] line widths,[8] spatial coherence,[9] and excitation energies[10] of these hybrid states may be altered in scientifically and technologically useful ways and, accordingly, have found utility in the pursuit of nanoscale organic lasing materials,[11] enhanced spectroscopic signatures,[12] and nearly thresholdless lasers.[13,14] Cavities strongly coupled to single optical emitters have also been considered for use in quantum information systems.[15−18]

While strong normal mode coupling has been widely investigated for *electronic-state* transitions, it is only very recently that cavity coupling to *vibrational* transitions was proposed and experimentally realized.[19−21] Work in this field has compared measured Rabi splittings to classical[19] and quantum-mechanical descriptions,[21] and the work by George et al.[22] greatly extended the experimental landscape by utilizing molecular liquids and higher order cavity modes. Vibrational

Received: June 11, 2015
Published: October 1, 2015

modes are particularly interesting because they involve nuclear motion along coordinates related to bond formation and cleavage. For instance, reaction pathways of ammonia,[23] nitrous oxide,[24] and deuterated water[25] on metal surfaces can be influenced through the excitation of selected vibrational bands. Examining vibrational modes in such coupled environments may be informative for realizing schemes for chemical control, which we term quantum-optical chemistry.

To use cavity coupling to control chemistry will require precise experimental control of the Rabi splitting in the cavity. In this work, we vary a range of parameters of the cavity−absorber system to experimentally verify theoretical treatments of the coupled system. Classical and quantum models predict that the Rabi splitting varies with the square root of the absorption coefficient (i.e., absorption per unit length, $\alpha_0 = 4\pi k\nu$, where k is the imaginary part of the complex refractive index) of the ensemble of absorbers. We experimentally confirm this dependence by varying the concentration of an absorber blended into a polymer host and span the weak and strong coupling regimes. Through this analysis, we estimate the impact of commonly applied simplifications to the expressions. This analysis leads to a simple expression for evaluating the critical concentration of an absorber required to attain strong coupling. The impact of cavity modal profile was investigated by varying mirror type (Au and dielectric stack) in cavities loaded with a thiocyanate (SCN^-) anion present as the counterion in a polycation polymer film. Somewhat counterintuitively, models predict that the Rabi splitting is independent of path length and, therefore, total absorbance. We experimentally verify this path length independence for coupling to $W(CO)_6$ and present the first results for solution-phase normal mode coupling, which is the environment most conducive for the study of chemical reaction.

■ METHODS

Cavity Preparation. Cavities used for the concentration dependence study were produced on undoped silicon wafers and comprised a HMDI:PMMA polymer blend placed between two metal films (20 nm Au, $R \approx 0.97$ in air). These cavities were designed and built to operate in the first order with an optical thickness of ~2.3 μm (optical thickness = index of refraction × physical thickness). The HMDI (4,4′-methylenebis(cyclohexyl isocyanate)) monomer was mixed at various volumetric concentrations into poly(methyl methacrylate) (PMMA) (molecular weight 950 kDa, 9% in anisole), forming solutions from which films were spun (~1250 rpm for 60 s, then baked at 110 °C for 60 s). HMDI concentrations in solution ranged from 0.625 to 20 vol %. Assuming evaporation of all anisole solvent from the spun and baked films, these solutions would produce films with HMDI content from ~6.5 to 74 vol %. Film thicknesses were measured with stylus profilometry. Witness films were spun directly on undoped silicon with no mirrors in order to extract HMDI film absorbance. Isocyanates react well with trace water, alcohols, or amines. These films were stable, e.g., less than 2% change in 2263 wavenumber isocyanate band intensity was noted during experiments. Several additional cavities were produced to explore the impact of mirror type (Au versus dielectric stack). These cavities comprised CaF_2 windows coated with either Au ($R \approx 0.97$) or a dielectric stack ($R \approx 94$, Universal Thin Films), then with a $PDDA^+SCN^-$ (poly(diallyldimethylammonium thiocyanate)) ionic polymer, and finally topped with a Au mirror. To explore path-length dependencies, fluid transmission cells composed of CaF_2 mirrors coated with dielectric stack mirrors were assembled with polymer spacing gaskets of various thicknesses (25−100 μm) then loaded with solutions of $W(CO)_6$ in *n*-hexane (2.5−10 mM). Poly(diallyldimethylammonium chloride) ($PDDA^+Cl^-$, M_w = 100−200 kDa, 20% wt solution in water, [26062-79-3]), sodium thiocyanate (NaSCN, 98%, [540-72-7]), anisole (99%, [100-66-3]), poly(methyl methacrylate) (M_w = 950 kDa, [9011-14-7]), and 4,4′-methylenebis(cyclohexyl isocyanate) (90%, mixture of isomers, [5124-30-1]) were all used as received from Sigma-Aldrich Chemicals, Inc. Spectra-Por BioTech Cellulose Ester (CE) dialysis membrane (catalogue no. 131273, nominal flat width = 24 mm; diameter = 15 mm, volume/length = 1.8 mL/cm, molecular weight cutoff (MWCO) = 8−10 kDa) was from Spectrum Laboratories Inc. (www.Spectrumlabs.com).

Preparation of $PDDA^+SCN^-$. A ~25−30 cm length of dialysis tubing was conditioned by soaking in H_2O for 60 min, after which H_2O was drained from the tubing and one end was sealed tightly with a clamp. A ~15.00 g portion of 20% wt $PDDA^+Cl^-$(aq) solution was transferred into the tubing, which was then sealed with a second clamp and sequentially submerged in fresh 500 mL volumes of gently stirred ~0.35 M NaSCN(aq) solutions for ~1, ~ 2, and ~15 h. After this time, the tube was sequentially submerged with gentle stirring in fresh 500 mL volumes of H_2O for 1 and 2 h, followed by a fresh 3 L volume of H_2O for ~19 h to remove excess NaSCN. The tube was opened, and the contents were frozen at −20 °C for 60 min in a Fisher Scientific Isotemp −20 °C freezer and then freeze-dried (~28 h) using a Virtis Benchtop K freeze-dryer system to remove the H_2O. Freeze-drying yielded 2.59 g of $PDDA^+SCN^-$ (theory = 3.42 g, yield ≅ 76%) as an off-white powder. Dissolution of ~0.08 g of the product in ~1 mL of H_2O, followed by addition of 2 mg of ferric chloride, instantly produced a blood red color indicative of the presence of thiocyanate.

Optical Measurements. Angle-dependent transmittance spectra were obtained in a Fourier-transform infrared (FTIR) spectrometer (Thermo Scientific with beam convergence full angle ~2.4°) equipped with a wire-grid polarizer and a home-built computer-controlled sample rotator. All measurements were taken in transmission mode and using s-polarization. For the concentration-dependent study, spectra were measured with 4 cm^{-1} resolution, which contributed negligibly (≲0.5 cm^{-1}) to the measured absorption line widths. For measurements of cavity-coupled $W(CO)_6$, spectra were acquired with a resolution of 0.5 cm^{-1}.

■ RESULTS AND DISCUSSION

As described previously,[19] and shown schematically in Figure 1a, samples consist of molecules of interest housed between two Au mirrors forming a ~1.6 μm Fabry−Pérot (FP) cavity whose resonance frequency may be tuned by varying experimental incident angle. When the cavity resonance coincides with the molecular absorption, coupling occurs. The splitting strongly depends on the absorbance per unit length.[1,26] To examine the system's response to varying absorption coefficient, a series of films was prepared with varying concentrations of the HDMI monomer in PMMA. Absorption spectra for witness samples (polymer films with no cavity mirrors) prepared for each concentration, Figure 1c, fit well to a Voigt function (Gaussian distribution of Lorentzian peaks).[27] The maximum absorption coefficient, α_0 (defined as

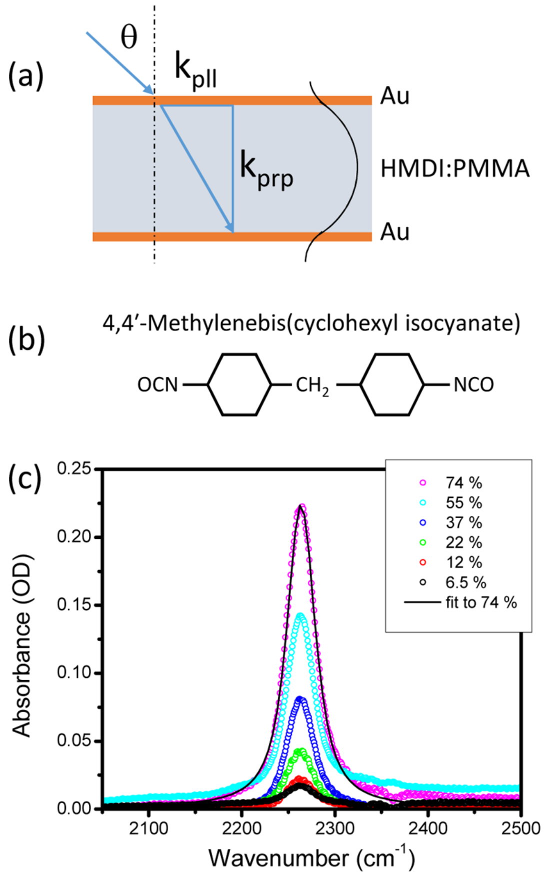

Figure 1. (a) Schematic of loaded Fabry−Perot cavity and conditions determining angle-dependent resonance. Increased incidence angle reduces normal component of the wavevector, k_{prp}, resulting in a blue-shift of cavity resonance. Subsequent dispersions in Figure 2 are plotted versus in-plane wave vector, k_{pll}. (b) Chemical structure of urethane monomer, HMDI, used as cavity load. (c) Absorption spectra of films (i.e., witness samples) consisting of varying concentration of HMDI in PMMA, highlighting isocyanate stretch at ∼2263 cm^{-1}. Curves are labeled with their approximate volumetric concentrations.

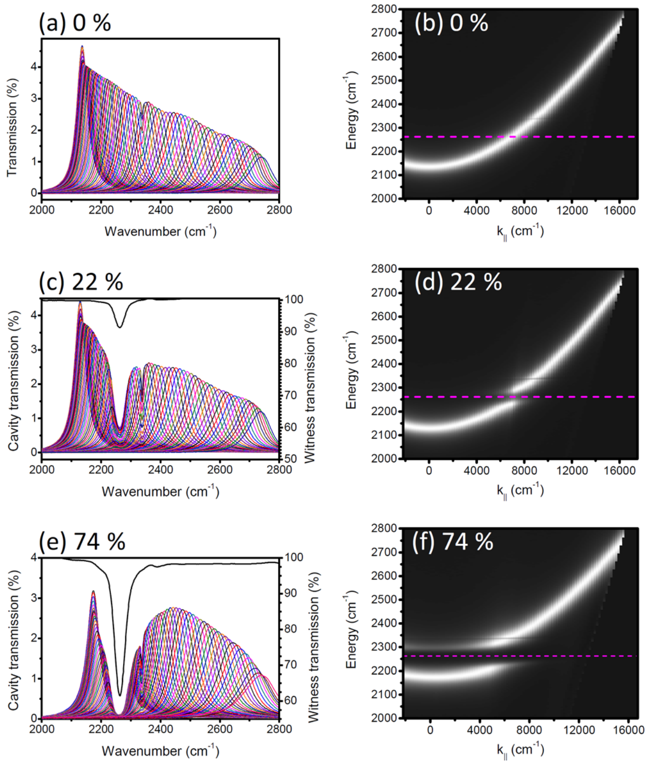

Figure 2. Angle-dependent transmission spectra of FP cavities loaded with no (a), low (c), and high (e) concentrations of HMDI in PMMA. The transmission spectra of witness samples are overlaid on these plots, showing correlation between absorption and anticrossing positions. Example dispersion contours for no (b), low (d), and high (f) concentrations. Panel (b) corresponds to the "empty" cavity dispersion and allows extraction of the uncoupled cavity width. Panels (d) and (f) demonstrate increased Rabi splitting with increased absorber strength (via increased concentration). Energy of unperturbed vibrational band is indicated by a pink dotted line.

$\alpha_0 = 4\pi k\nu_0$, in units of cm^{-1}, and not to be confused with the molar attenuation or molar extinction coefficient defined as $\varepsilon = A/(CL)$ in Beer's law), occurs at the absorption frequency ($\nu_0 \approx 2263\ \mathrm{cm}^{-1}$) for the asymmetric isocyanate stretch in HMDI (Figure 1b). Detailed procedures and example fits are found in the Supporting Information. Film concentrations of 22−74 vol % yielded consistent widths (Lorentzian width = 26.7 ± 0.6 cm^{-1}; Gaussian width = 17.1 ± 0.8 cm^{-1}). Accordingly, the homogeneous line width of the molecule, Γ_{H}, will be assigned as 26.7 cm^{-1} in the analytical comparisons to data. The two lowest HDMI concentrations (red and black curves in Figure 1c) yielded Lorentzian widths ∼10 cm^{-1} broader. The cavity line width, Γ_{cav}, was measured directly from a pure PMMA cavity and found to be 50 cm^{-1}, corresponding to a cavity quality factor of ∼45 (see Supporting Information).

Transmission spectra were acquired as a function of incident angle from −10° to +70° at 1° spacing. Raw angle-dependent spectra are shown in Figure 2a, c, and e and converted to $k_{\|}$-space contours in b, d, and f. Due to acquisition of the data in an off-normal measurement, the two hybridized modes assume different internal wavevectors for any non-normal angle of incidence, a consequence of the strong frequency dependence of the refractive index. To reflect the coherence giving rise to the hybridization, angular-dispersion data must be replotted versus the in-plane component of the wavevector.[2] The in-plane component is the same both inside and outside the cavity and is given by $k_{\|} = k_0 \sin(\theta)$, where θ is the angle of incidence and k_0 is the free space wavevector $2\pi\bar{\nu}$. Figure 2b shows the experimental dispersion of the "empty" cavity (containing 0% HDMI in PMMA). Two more example dispersion contours are presented, Figures 2d and f, and provide examples of cavities with weakly and strongly absorbing cavity loads (i.e., low and high concentrations of HDMI) exhibiting small and large anticrossings, respectively. Anticrossing occurs at the frequency of the vibrational mode of the uncoupled isocyanate stretch at ∼2263 cm^{-1}, which is marked by a dotted pink line, creating distinct upper and lower branches of the cavity dispersion. The minimum branch separation is the Rabi splitting and increases with absorber concentration (compare Figure 2d and f). In general, at low $k_{\|}$, the upper branch (UB) near 2300 cm^{-1} is primarily of vibrational character, while the lower branch (LB) near 2200 cm^{-1} is mainly of cavity character. As incident angle, and therefore $k_{\|}$, is increased, the cavity resonance tunes through the unperturbed vibrational absorption frequency and induces mode hybridization, leading to an avoided crossing when the cavity becomes resonant with the isocyanate stretch absorption. At high $k_{\|}$, the character of the two branches switches, so that the UB disperses rapidly with angle in accord with FP-cavity behavior. The weak feature at ∼2340 cm^{-1} is associated with background CO_2. The full set of dispersion contours is included in the Supporting Information.

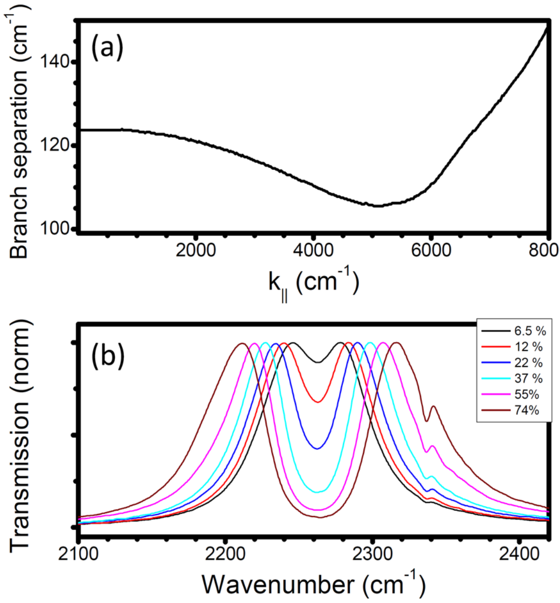

Figure 3. (a) Example data of measured branch separation as a function of in-plane wavevector, $k_{||}$. Minimum separation is the Rabi splitting (106 cm^{-1} in this case, corresponding to 74% HMDI). (b) Transmission spectra taken at conditions of best coupling determined as the $k_{||}$ value where branch separation is minimum. Although the peaks separate further as HMDI concentration is increased, the qualitative form of the spectra is consistent. Small feature at ~2340 cm^{-1} is associated with a CO_2 stretch present in the background.

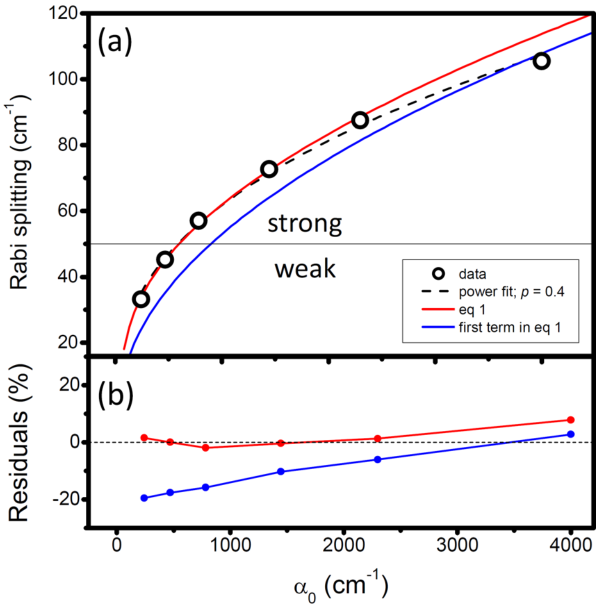

Figure 4. (a) Measured Rabi splitting (black circles) as a function of absorption coefficient along with three analytical treatments. The solid horizontal line indicates the transition between weak and strong coupling. A simple power law fit (black dashed curve and defined as $\Omega = A^*{\alpha_0}^p$) deviates slightly from a square root dependence with $p = 0.4$. The full expression from Savona et al., ref 30 (red curve), provides excellent agreement, with no free parameters. Simplifying this expression through neglect of the secondary terms (blue curve) results in poorer agreement and worsens at low absorber strength. (b) Plot of error between analytical treatments and raw data as percentage of measured Rabi splitting.

With the k-space dispersion contours in hand, the Rabi splitting may be determined by plotting the energy separation between the upper and lower branches as a function of $k_{||}$. The minimum separation is the Rabi splitting, which occurs near $k_{||} = 5000$ cm^{-1} in the data shown for the 74% HDMI sample in Figure 3a. The $k_{||}$ position of this minimum identifies the condition where maximum coupling occurs. We now plot the transmission spectra at strongest coupling in Figure 3b and the Rabi splitting as a function of absorption coefficient, α_0, in Figure 4a. The transmission spectra are labeled with their approximate HMDI vol %, which serves as an estimate of the absorber content. As absorber concentration increases, the two peaks split further and symmetrically from the absorber frequency (~2263 cm^{-1}). Each of the two peaks approximately follows an asymmetric Lorentzian shape with a tail extending away from the center frequency, similar to profiles measured for quantum wells[1] and organic dye molecules[28] coupled to confined optical modes. We see no qualitative change in the overall line shape as absorber concentration is varied. The splitting magnitudes range from 33 to 106 cm^{-1}, spanning the so-called strong and weak coupling regimes with the maximum splitting ~5% of the resonance energy. Strong coupling requires the splitting to be larger than both of the two line widths (i.e., $\Omega > \Gamma_H, \Gamma_{cav}$). When this condition is met, energy can oscillate coherently between the two mixed states before dissipating from the system.[29] The Rabi splitting values are plotted in Figure 4a versus the homogeneous absorption coefficient as extracted from Voigt fits of the witness films, Figure 1c. The splitting observed in transmission through such a cavity is expressed as[30]

$$\Omega_T = \sqrt{\sqrt{\left(\frac{\alpha_0\Gamma_H}{2\pi n_B}\right)^2 + \frac{\alpha_0\Gamma_H}{\pi n_B}\Gamma_H(\Gamma_H + \Gamma_{cav})} - {\Gamma_H}^2} \tag{1}$$

where n_B is the "background" refractive index and other terms are as defined earlier. For systems with large α_0 values, this expression is dominated by the first term on the right-hand side; thus a square-root dependence of Rabi splitting on absorber concentration is often reported.[31−33] This dependence on absorber concentration has been noted before and can be seen from the above expression since $\alpha_0 = 2.303A_{max}/L = 2.303\varepsilon C$, where ε is the (decadic, i.e., common log) molar extinction coefficient and C is the molecular concentration.

In the following discussion, we will compare the experimental data set to analytical treatments consisting of an empirical functionality (simple power law), the full analytical treatment offered by eq 1, and the often-applied square-root dependence, which amounts to a simplification of eq 1 where only the first term is considered. First, the raw data are fit to a simple power law, $\Omega = A{\alpha_0}^p$, which yields $p = 0.4$ (black dotted curve). This deviates from the functionality of $p = 0.5$ obtained when considering only the first term (eq 1). Forcing $p = 0.5$ results in a significantly worse fit (R^2 value degrades from 0.996 to 0.946; see Supporting Information). This suggests the secondary terms in eq 1 contribute measurably to this extended data set. Next, we overlay two analytical treatments directly on the raw data in Figure 4a. The red curve is associated with the full expression of eq 1, while the blue curve includes only the first term in eq 1 and represents the often-applied square-root dependence. In both cases, no fitting parameters were used since all cavity and absorber characteristics may be measured independently (see Supporting Information for details). The agreement between the data (black circles) and the full transmission expression[30] (eq 1; red curve) is striking. The largest deviation, ~7 cm^{-1}, occurs at the maximum concentration, while the rest of the values predicted by eq 1 are within 2% of the experimental results. The agreement between eq 1 and the raw data demonstrates that eq 1 adequately describes the experiment even through the transition to the weak coupling regime (i.e., $\Omega < \Gamma_H, \Gamma_{cav}$) represented by the two lowest concentrations. Using only the first term in eq 1 (blue curve) produces qualitative agreement with the data but diverges in the low-concentration regime, with errors as high as ~23% occurring near the smallest splitting.

Next we systematically evaluate the significance of the secondary terms in eq 1 as a function of system parameters chosen to bracket our experimental values. In Figure 5, we plot the contribution of the second and third terms under the square root on the right-hand side of eq 1 relative to the total predicted Rabi splitting. In (a) absorber width is fixed with varying cavity line width, while in (b) the cavity width is fixed and absorber width varied. The blue curve in both is identical and matches our experimental conditions. With Γ_H fixed at 26.7 cm^{-1}, Figure 5a, the relative strength of the correction terms becomes more significant with increased cavity line width, attains a maximum at relatively low absorption coefficient, $\alpha_0 \approx$ 300–600 cm^{-1}, and is as large as 12 cm^{-1} (~30% of the predicted splitting at that condition). For cavities operating in the strong coupling regime, the corrections are smaller, ranging from ~1 to 10 cm^{-1} (<15% of the predicted splitting). The relative strength of the correction terms as a function of absorber width, Γ_H, is quite different. The magnitude of these contributions increases as absorber line width decreases, opposite of the trend revealed above, due to the reduced dominance of the first term on the right-hand side of eq 1 as Γ_H is reduced. In all cases, the strongest deviations occur at small absorber concentrations due to the weakening of the first term in eq 1. Finally, we reproduce and add the relative errors from Figure 4b associated with neglect of the secondary terms in eq 1 (i.e., the square-root simplification) into Figure 5a. These errors are similar to those occurring when ignoring secondary terms in eq 1. This analysis shows that the errors associated with neglect of the secondary terms are <15% in the strong coupling regime and are considerably smaller for narrow cavity line widths, suggesting that it is reasonable to adopt the simplified expression when estimating coupling strengths to different molecular vibrations. Therefore, we present a criterion for estimating the absorber concentration required to achieve strong coupling based on the vibration's molar extinction coefficient and line width. We take just the first term in eq 1, substitute in appropriate expressions for the absorption coefficient, assume that the cavity line width is greater than the infrared absorption width of the molecule, and find that the threshold of achieving strong coupling is $\varepsilon C \Gamma_H / 2.7 \Gamma_C^2 n_B \geq 1$ with all terms as previously defined (full derivation found in the Supporting Information). With the further simplification of setting the line widths equal ($\Gamma_H = \Gamma_C$), one may predict the concentration needed to achieve strong coupling as $C \geq 2.7 n_B \Gamma_H / \varepsilon$. As an example, the concentration of thiocyanate ($\varepsilon = 700\ \text{M}^{-1}\ \text{cm}^{-1}$, $\Gamma_H = 26.5\ \text{cm}^{-1}$) in water necessary to achieve strong coupling is 0.4 M. This is ~10 times lower than the solubility limit, revealing that it is a good candidate for strong coupling.

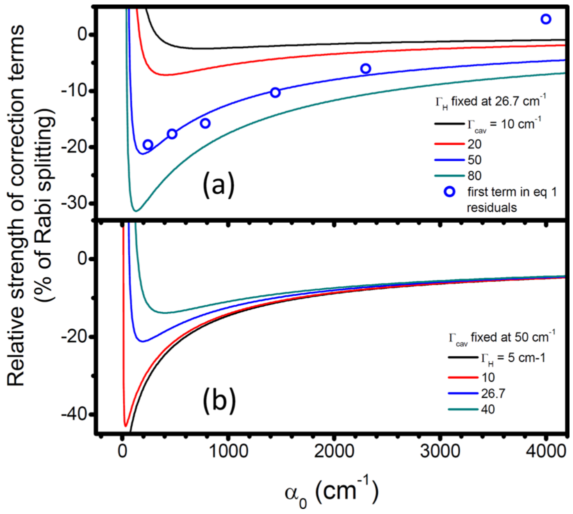

Figure 5. Evaluation of the importance of secondary terms in eq 1 as a function of absorption coefficient and line widths. All solid curves are calculated as the strength of the secondary terms in eq 1 relative to the total splitting predicted. In (a), absorber line width is fixed at the experimentally determined value and cavity line width is varied and shows the greatest deviation for large cavity line widths. Blue circles in (a) correspond to deviation between measured data and simplified eq 1 (i.e., neglecting secondary terms). In (b), cavity line width is fixed and absorber line width is varied. In this case, the greatest deviation occurs for narrow absorption widths. In all cases, deviations are generally more significant for weak absorption coefficient, α_0, reflecting the weakened dominance of the first term in eq 1.

As established above, the Rabi splitting may be controlled via the absorption coefficient of the vibrational band in the cavity. However, the effect of mode overlap is not represented in eq 1. Here we evaluate the impact of mode overlap by implementing two different mirror types. Dielectric Bragg mirrors, consisting of a stack of dissimilar dielectrics, have the advantage of higher transmission needed for low signal strength transient measurements. However, mode extension into the dielectric stack reduces the overlap between the cavity mode and the molecules housed between the mirrors. In order to investigate this effect, we measure coupling to the CN stretch near 2052 cm^{-1} in thiocyanate substituted into an ionic polymer ($\text{PDDA}^+\text{SCN}^-$; see Methods). The spectra and dynamics of the CN stretch of thiocyanate have been widely studied in solution.[34−36] In the polymer, the band fits well to a Lorentzian centered at 2052.0 cm^{-1} with $\Gamma_H = 26.5\ \text{cm}^{-1}$. A comparison of cavities formed by two metal mirrors (Figure 6a,b) and one metal and one dielectric mirror (Figure 6c,d; dielectric mirror exhibits 94% reflectivity in air, from Universal Thin Films) is presented. In both cases, the film was spun to a thickness of ~1.68 μm in order to operate the cavity in the first-order. Although the dispersions of the two cavities are qualitatively similar, the extracted Rabi splitting is considerably larger for the metal–metal cavity (Ω = 131 cm^{-1}) than for the metal–dielectric cavity (98 cm^{-1}). Both cavities are in the strong-coupling regime. The notable ~30% increase in Rabi splitting for the metal–metal cavity is due to stronger optical field confinement between the metal mirrors. Significant field penetration into dielectric mirrors[30,37] results in less interaction between the absorbers and the cavity mode, and, therefore, a reduced Rabi splitting as has been observed for cavities coupled to organic dye molecules absorbing at $\lambda \approx 1.5$ μm (~6667 cm^{-1}).[38]

DOI: 10.1021/acsphotonics.5b00324
ACS Photonics 2015, 2, 1460−1467

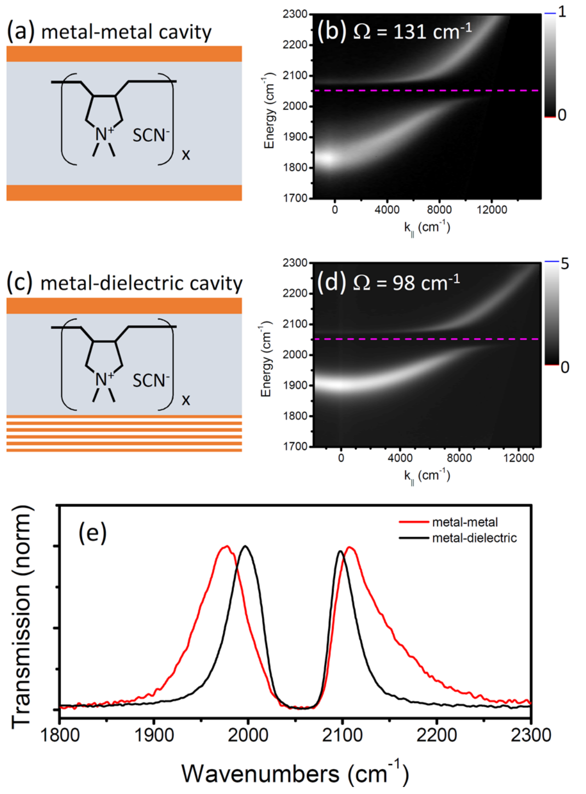

Figure 6. Influence of cavity mirror type (a and c) is demonstrated by comparing the measured dispersions of a metal−metal cavity (b) and a metal−dielectric cavity (d) containing identical loads (same film thickness and absorber content). The metal−dielectric cavity (d) produces narrower line widths, higher transmission, and reduced Rabi splitting due to mode penetration into the dielectric mirror and, therefore, weakened mode overlap. Panel (e) plots the spectrum at strongest coupling, revealing the narrower widths and weaker coupling associated with the metal−dielectric cavity. Scale on the contour plots is in percent transmission.

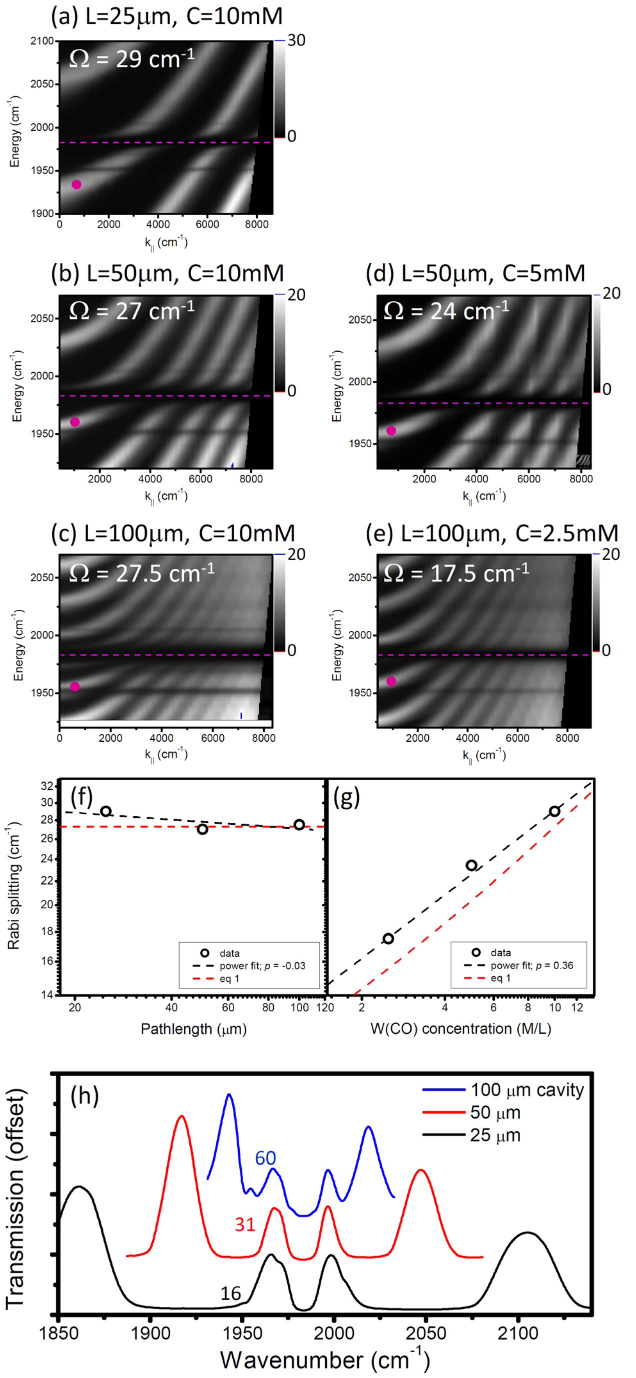

Figure 7. Concentration- and thickness-dependent dispersions for $W(CO)_6$ in hexane. (a−c) Response for different cavity thickness with concentration scaled to maintain fixed absorbance. (a, d, e) Response for different thicknesses and varying concentration. Pink dots indicate mode used for extraction of Rabi splitting that is plotted in (f) and (g) and demonstrate pathlength independence of the Rabi splitting. Simple power law fits (black dashed) and values predicted by eq 1 (red dashed curves) are included. (h) Plots of transmission for different cavity thicknesses with mode index identified.

Additionally, the cavity quality factor (Figure 6e), measured far from strong coupling, of the metal−metal cavity ($Q = 20$, $\Gamma = 93$ cm^{-1}) is lower than for the metal−dielectric cavity ($Q = 34$, $\Gamma = 56$ cm^{-1}), although we recognize that the cavity quality factor is a function of reflectivity rather than mirror type and can be extended to thicker cavity via the finesse, $\mathcal{F} = \mathrm{FSR}/\Gamma_{\mathrm{cav}}$, where FSR is the free spectral range. Although preliminary, this exercise demonstrates the significant role that cavity design can have on cavity−molecule interactions and further demonstrates the broad applicability of this technique through the use of a substituted ionic polymer as the cavity load.

In contrast to typical linear absorption and Beer's law, where the total absorbance determines the measured response, the coupling strength (i.e., Rabi splitting) discussed in this work follows the absorbance per unit length (i.e., absorber concentration). According to eq 1, increasing the FP cavity path length, while maintaining a fixed absorber concentration, will increase the total absorbance, but should not increase the coupling strength. In this final example, Figure 7, we probe this predicted path length independence by loading solutions of $W(CO)_6$/*n*-hexane (the carbonyl stretch of $W(CO)_6$ occurs at 1983 cm^{-1}) between two dielectric-coated CaF_2 windows. The path length between the mirrors and solution concentration were varied in order to generate two sample sets. In the first set, cavity thickness was varied from 25 to 100 μm while maintaining a fixed 10 mM solution concentration (Figure 7a−c), resulting in a total absorbance that scales with cavity thickness but an absorbance per unit length (i.e., absorption coefficient) that remains constant. In the second set, cavity thickness was also varied from 25 to 100 μm, but the solution concentration was scaled to maintain a constant total absorbance (Figure 7a, d, e). All of the contours exhibit multiple cavity modes owing to the increased cavity pathlengths, which will be discussed further below. Although multiple cavity modes interact with the vibrational mode, the Rabi splittings were extracted for the first mode seen to interact with the absorber (mode is labeled with a pink dot). The extracted splittings are plotted in Figures 7f and g and show that when the path length is increased with a fixed solution concentration (Figure 7f), the Rabi splitting is essentially unchanged (fitted power law exponent $p = 0.03$; black dotted curve) even though the total absorbance changes by a factor of 4. Extrapolating this result suggests that strong coupling may be achieved in nanoscale resonators, such as phonon polariton structures or metamaterial surfaces, as long as absorber concentration is maintained, despite the fact that the total absorbance due to these molecules would be miniscule. Turning one's attention to the case of increased path length with constant absorbance (Figure 7g), the extracted Rabi splitting increases with increased absorber concentration even though total absorbance for these samples has been fixed. This is confirmation of the concentration-dependent response predicted by eq 1. These data, Figure 7g, yield a fitted power law exponent $p = 0.36 \pm 0.03$, which is similar to the $p = 0.4$ found above for the more comprehensive urethane data set (Figure 4). The Rabi splitting predicted via eq 1 is added (red dotted curves) based on a molecular line width of $\Gamma_H = 3.6$ cm^{-1}, a molar extinction coefficient $\varepsilon = 7.08 \times 10^4$ L mol^{-1} cm^{-1} of $W(CO)_6$ measured for a 5 mM solution, and a cavity line width $\Gamma_{cav} = 10$ cm^{-1}.

Although the strength of the coupling is not increased with thicker cavities, new opportunities may reside in their use. Cavity line width is narrowed for higher order modes (see Figure 7h), allowing one to match vibration and cavity lifetimes in these coupled systems. Also, new phenomena, such as vibration-mediated energy exchange between different cavity modes, may be accessible in these higher order cavities. In all of the dispersions, one sees multiple cavity modes coupled to the $W(CO)_6$. This phenomenon is similar to the polariton ladder demonstrated for coupled excitonic systems,[39] which showed simultaneous strong coupling between excitons and multiple cavity modes and simultaneous polariton population in multiple cavity modes. The free spectral range (FSR), which is the separation between resonant transmission peaks, depends on cavity length, L. Adjacent resonant transmission peaks give FSRs of 122, 64, and 33 cm^{-1} for the 25, 50, and 100 μm thick cavities, respectively. Relating the FSR (in cm^{-1}) to cavity thickness (in μm) according to $L = 5000/n_B\text{FSR}$, where $n_B = 1.44$ is the background refractive index for hexane, yields cavity thicknesses of $L = 28$, 54, and 105 μm, in close agreement with the nominal spacer dimensions. Rearranging the resonant condition for an FP cavity[40] and assuming no phase shift upon reflection at the dielectric mirrors give the operating mode of a cavity as $m = L\nu_m n_B/5000$, where ν_m is the resonant frequency and all other terms are as previously defined. This allows one to identify the order of the mode coupled to the $W(CO)_6$ carbonyl vibration. We have noted the mode order near the lower polariton branches for the three cavity thicknesses in the spectra plotted in Figure 7h, corresponding to three cavity thicknesses with a fixed solution concentration. The mode number scales up with cavity thickness; however, the observed splitting is essentially unchanged for these fixed concentration samples. These results show that, in addition to molecular liquids, strong coupling can occur in liquid solutions where chemical reactions are likely to be studied.

■ CONCLUSIONS

Through variation of absorber concentration, we have produced coupling between a Fabry−Pérot cavity and molecular vibrations that spans the weak and strong coupling regimes. The Rabi splitting ranges from slightly less than (33 cm^{-1}) to twice (106 cm^{-1}) the unperturbed cavity line width (50 cm^{-1}). The experimentally determined Rabi splitting values are in excellent agreement with an analytical expression derived for classical coupled oscillators. Based on a simple expression for evaluating the coupling strength between an absorber and a cavity, a criterion for selecting molecules suitable for strong coupling was developed. The impact of optical mode distribution on coupling strength is demonstrated through variation of cavity mirror type. Dielectric stack mirrors provide the benefits of higher transmissivity for a given quality factor; however, coupling strength is decreased due to greater mode penetration into the mirror relative to that occurring for metal mirrors, resulting in reduced modal overlap with the molecular cavity load. Finally, the path length independence of the coupling strength was demonstrated for higher order cavities filled with liquid solutions. This work strives to develop an understanding of the roles of various system parameters (molecular and cavity line widths, modal distribution, film absorption coefficient) on vibrational−cavity coupling and validate empirical and analytical descriptions of such coupling with the hope that this phenomenon might enable currently unreachable chemistries.

■ ASSOCIATED CONTENT

Ⓢ Supporting Information

The Supporting Information is available free of charge on the ACS Publications website at DOI: 10.1021/acsphotonics.5b00324.

Additional information (PDF)

■ AUTHOR INFORMATION

Corresponding Author

*E-mail: blake.simpkins@nrl.navy.mil.

Notes

The authors declare no competing financial interest.
§National Research Council Postdoctoral Researcher.

■ ACKNOWLEDGMENTS

We thank Dr. J. P. Long and H. D. Ladouceur for guidance and the National Research Council for administering the postdoctoral program. This research was funded through the Office of Naval Research.

■ REFERENCES

(1) Khitrova, G.; Gibbs, H. M.; Jahnke, F.; Kira, M.; Koch, S. W. Nonlinear optics of normal-mode-coupling semiconductor microcavities. *Rev. Mod. Phys.* **1999**, *71*, 1591−1639.

(2) Agranovich, V. M.; Litinskaia, M.; Lidzey, D. G. Cavity polaritons in microcavities containing disordered organic semiconductors. *Phys. Rev. B: Condens. Matter Mater. Phys.* **2003**, *67*, 085311.

(3) Fofang, N. T.; Grady, N. K.; Fan, Z.; Govorov, A. O.; Halas, N. J. Plexciton Dynamics: Exciton Plasmon Coupling in a J-Aggregate-Au Nanoshell Complex Provides a Mechanism for Nonlinearity. *Nano Lett.* **2011**, *11*, 1556−1560.

(4) Reithmaier, J. P.; Sęk, G.; Löffler, A.; Hofmann, C.; Kuhn, S.; Reitzenstein, S.; Keldysh, L. V.; Kulakovskii, V. D.; Reinecke, T. L.; Forchel, A. Strong coupling in a single quantum dot–semiconductor microcavity system. *Nature* **2004**, *432*, 197–200.

(5) Yoshie, T.; Scherer, A.; Hendrickson, J.; Khitrova, G.; Gibbs, H. M.; Rupper, G.; Ell, C.; Shchekin, O. B.; Deppe, D. G. Vacuum Rabi splitting with a single quantum dot in a photonic crystal nanocavity. *Nature* **2004**, *432*, 200–203.

(6) Gomez, D.; Lo, S. S.; Davis, T. J.; Hartland, G. V. Picosecond Kinetics of Strongly Coupled Excitons and Surface Plasmon Polaritons. *J. Phys. Chem. B* **2013**, *117*, 4340–4346.

(7) Norris, T. B.; Rhee, J.-K.; Sung, C.-Y.; Arakawa, Y.; Nishioka, M.; Weisbuch, C. Time-resolved vacuum Rabi oscillations in a semiconductor quantum microcavity. *Phys. Rev. B: Condens. Matter Mater. Phys.* **1994**, *50*, 14663–14666.

(8) Houdré, R.; Stanley, R. P.; Ilegems, M. Vacuum-field Rabi splitting in the presence of inhomogeneous broadening: Resolution of a homogeneous linewidth in an inhomogeneously broadened system. *Phys. Rev. A: At., Mol., Opt. Phys.* **1996**, *53*, 2711–2715.

(9) Shi, L.; Hakala, T. K.; Rekola, H. T.; Martikainen, J. P.; Moerland, R. J.; Törmä, P. Spatial Coherence Properties of Organic Molecules Coupled to Plasmonic Surface Lattice Resonances in the Weak and Strong Coupling Regimes. *Phys. Rev. Lett.* **2014**, *112*, 153002.

(10) Hutchison, J. A.; Schwartz, T.; Genet, C.; Devaux, E.; Ebbesen, T. W. Modifying Chemical Landscapes by Coupling to Vacuum Fields. *Angew. Chem., Int. Ed.* **2012**, *51*, 1592–1596.

(11) Tischler, J. R.; Scott Bradley, M.; Zhang, Q.; Atay, T.; Nurmikko, A.; Bulović, V. Solid state cavity QED: Strong coupling in organic thin films. *Org. Electron.* **2007**, *8*, 94–113.

(12) Shalabney, A.; George, J.; Hiura, H.; Hutchison, J. A.; Genet, C.; Hellwig, P.; Ebbesen, T. W. Enhanced Raman Scattering from Vibro-Polariton Hybrid States. *Angew. Chem., Int. Ed.* **2015**, *54*, 7971–7975.

(13) Yokoyama, H. Physics and Device Applications of Optical Microcavities. *Science* **1992**, *256*, 66–70.

(14) Yokoyama, H.; Suzuki, M.; Nambu, Y. Spontaneous emission and laser oscillation properties of microcavities containing a dye solution. *Appl. Phys. Lett.* **1991**, *58*, 2598–2600.

(15) Englund, D.; Shields, B.; Rivoire, K.; Hatami, F.; Vučković, J.; Park, H.; Lukin, M. D. Deterministic Coupling of a Single Nitrogen Vacancy Center to a Photonic Crystal Cavity. *Nano Lett.* **2010**, *10*, 3922–3926.

(16) Park, Y.-S.; Cook, A. K.; Wang, H. Cavity QED with Diamond Nanocrystals and Silica Microspheres. *Nano Lett.* **2006**, *6*, 2075–2079.

(17) Kasprzak, J.; Richard, M.; Kundermann, S.; Baas, A.; Jeambrun, P.; Keeling, J. M. J.; Marchetti, F. M.; Szymańska, M. H.; André, R.; Staehli, J. L.; Savona, V.; Littlewood, P. B.; Deveaud, B.; Dang, L. S. Bose–Einstein condensation of exciton polaritons. *Nature* **2006**, *443*, 409–414.

(18) Khitrova, G.; Gibbs, H. M.; Kira, M.; Koch, S. W.; Scherer, A. Vacuum Rabi splitting in semiconductors. *Nat. Phys.* **2006**, *2*, 81–90.

(19) Mason, J. A.; Allen, G.; Podolskiy, V. A.; Wasserman, D. Strong Coupling of Molecular and Mid-Infrared Perfect Absorber Resonances. *IEEE Photonics Technol. Lett.* **2012**, *24*, 31–33.

(20) Long, J. P.; Simpkins, B. S. Coherent Coupling between a Molecular Vibration and Fabry–Perot Optical Cavity to Give Hybridized States in the Strong Coupling Limit. *ACS Photonics* **2015**, *2*, 130–136.

(21) Shalabney, A.; George, J.; Hutchison, J.; Pupillo, G.; Genet, C.; Ebbesen, T. W. Coherent coupling of molecular resonators with a microcavity mode. *Nat. Commun.* **2015**, *6*, 5981.

(22) George, J.; Shalabney, A.; Hutchison, J. A.; Genet, C.; Ebbesen, T. W. Liquid-Phase Vibrational Strong Coupling. *J. Phys. Chem. Lett.* **2015**, *6*, 1027–1031.

(23) Pascual, J. I.; Lorente, N.; Song, Z.; Conrad, H.; Rust, H.-P. Selectivity in vibrationally mediated single-molecule chemistry. *Nature* **2003**, *423*, 525–528.

(24) Prybyla, J. A.; Heinz, T. F.; Misewich, J. A.; Loy, M. M. T.; Glownia, J. H. Desorption induced by femtosecond laser pulses. *Phys. Rev. Lett.* **1990**, *64*, 1537–1540.

(25) Jiang, B.; Xie, D.; Guo, H. Vibrationally mediated bond selective dissociative chemisorption of HOD on Cu(111). *Chem. Sci.* **2013**, *4*, 503–508.

(26) Dintinger, J.; Klein, S.; Bustos, F.; Barnes, W. L.; Ebbesen, T. W. Strong Coupling Between Surface Plasmon-Polaritons and Organic Molecules in Subwavelength Hole Arrays. *Phys. Rev. B: Condens. Matter Mater. Phys.* **2005**, *71*, 035424.

(27) Wertheim, G. K.; Butler, M. A.; West, K. W.; Buchanan, D. N. Determination of Gaussian and Lorentzian Content of Experimental Line-Shapes. *Rev. Sci. Instrum.* **1974**, *45*, 1369–1371.

(28) Dintinger, J.; Klein, S.; Bustos, F.; Barnes, W. L.; Ebbesen, T. W. Strong coupling between surface plasmon-polaritons and organic molecules in subwavelength hole arrays. *Phys. Rev. B: Condens. Matter Mater. Phys.* **2005**, *71*, 035424.

(29) Törmä, P.; Barnes, W. L. Strong coupling between surface plasmon polaritons and emitters: a review. *Rep. Prog. Phys.* **2015**, *78*, 013901.

(30) Savona, V.; Andreani, L. C.; Schwendimann, P.; Quattropani, A. Quantum well excitons in semiconductor microcavities: Unified treatment of weak and strong coupling regimes. *Solid State Commun.* **1995**, *93*, 733–739.

(31) Hakala, T. K.; Toppari, J. J.; Kuzyk, A.; Pettersson, M.; Tikkanen, H.; Kunttu, H.; Törmä, P. Vacuum Rabi Splitting and Strong-Coupling Dynamics for Surface-Plasmon Polaritons and Rhodamine 6G Molecules. *Phys. Rev. Lett.* **2009**, *103*, 053602.

(32) Canaguier-Durand, A.; Devaux, E.; George, J.; Pang, Y.; Hutchison, J. A.; Schwartz, T.; Genet, C.; Wilhelms, N.; Lehn, J.-M.; Ebbesen, T. W. Thermodynamics of Molecules Strongly Coupled to the Vacuum Field. *Angew. Chem., Int. Ed.* **2013**, *52*, 10533–10536.

(33) Balci, S.; Kocabas, C.; Ates, S.; Karademir, E.; Salihoglu, O.; Aydinli, A. Tuning surface plasmon-exciton coupling via thickness dependent plasmon damping. *Phys. Rev. B: Condens. Matter Mater. Phys.* **2012**, *86*, 235402.

(34) Dahl, K.; Sando, G. M.; Fox, D. M.; Sutto, T. E.; Owrutsky, J. C. Vibrational spectroscopy and dynamics of small anions in ionic liquid solutions. *J. Chem. Phys.* **2005**, *123*, 084504.

(35) Lenchenkov, V.; She, C.; Lian, T. Vibrational Relaxation of CN Stretch of Pseudo-Halide Anions (OCN^-, SCN^-, and $SeCN^-$) in Polar Solvents. *J. Phys. Chem. B* **2006**, *110*, 19990–19997.

(36) Ohta, K.; Tominaga, K. Vibrational population relaxation of thiocyanate ion in polar solvents studied by ultrafast infrared spectroscopy. *Chem. Phys. Lett.* **2006**, *429*, 136–140.

(37) Skolnick, M. S.; Fisher, T. A.; Whittaker, D. M. Strong coupling phenomena in quantum microcavity structures. *Semicond. Sci. Technol.* **1998**, *13*, 645–669.

(38) Hobson, P. A.; Barnes, W. L.; Lidzey, D. G.; Gehring, G. A.; Whittaker, D. M.; Skolnick, M. S.; Walker, S. Strong exciton–photon coupling in a low-Q all-metal mirror microcavity. *Appl. Phys. Lett.* **2002**, *81*, 3519–3521.

(39) Coles, D. M.; Lidzey, D. G. A ladder of polariton branches formed by coupling an organic semiconductor exciton to a series of closely spaced cavity-photon modes. *Appl. Phys. Lett.* **2014**, *104*, 191108.

(40) Born, M.; Wolf, E. *Principles of Optics*; Pergamon: New York, 1980.